Formation of solid Kr nanoclusters in MgO

van Huis, MA; van Veen, A; Schut, H; Kooi, BJ; De Hosson, JTM

Published in:
Physical Review. B: Condensed Matter and Materials Physics

DOI:
10.1103/PhysRevB.67.235409

Formation of solid Kr nanoclusters in MgO

M. A. van Huis, A. van Veen, and H. Schut
Interfaculty Reactor Institute, Delft University of Technology, Mekelweg 15, NL 2629 JB Delft, The Netherlands

B. J. Kooi and J. Th. M. De Hosson
Materials Science Centre, University of Groningen, Nijenborgh 4, NL 9747 AG Groningen, The Netherlands
(Received 5 October 2002; revised manuscript received 31 March 2003; published 10 June 2003)

The phenomenon of positron confinement enables us to investigate the electronic structure of nanoclusters embedded in host matrices. Solid Kr nanoclusters are a very interesting subject of investigation because of the very low predicted value of the positron affinity of bulk Kr. In this work, positron trapping in solid Kr nanoclusters embedded in MgO is investigated. The Kr nanoclusters were created by means of 280 keV Kr ion implantation in single crystals of MgO(100) and subsequent thermal annealing at a temperature of 1100 K. The nanoclusters were observed by cross-sectional transmission electron microscopy in high-resolution mode. The fcc Kr nanoclusters are rectangularly shaped with sizes of 2 to 5 nm and are in a cube-on-cube orientation relationship with the MgO host matrix. From the Moiré fringes in high-resolution recordings, the lattice parameter of the solid Kr was deduced and found to vary from 5.3 to 5.8 Å. The corresponding pressures are 0.6–2.5 GPa as found using the Ronchi equation of state. The relationship between lattice parameter and cluster size was investigated and it was found that the lattice parameter increases linearly with increasing nanocluster size. The defect evolution during annealing was monitored by means optical absorption spectroscopy and positron beam analysis. No evidence of positron trapping was found despite the very low positron affinity of solid Kr. Alternative definitions of the positron affinity are proposed for application to insulator materials.

DOI: 10.1103/PhysRevB.67.235409 PACS number(s): 61.46.+w, 68.65.−k, 71.60.+z, 78.70.Bj

I. INTRODUCTION

Recently, great advances have been made in the investigation of the electronic structure of metallic nanoclusters by means of positron annihilation spectroscopy. When certain requirements with respect to the positron affinity are fulfilled, the vast majority of the positrons is trapped in embedded nanoclusters, thereby becoming a self-seeking probe for nanocluster material. When a positron technique such as two-dimensional angular correlation of annihilation radiation (2D-ACAR) is used, the positrons reveal the electronic structure of the nanoclusters. This discovery is very interesting since below a certain cluster size, all material properties of the nanocluster start to change: structural phase transformations, metal-insulator transitions, modification of optical properties, and widening of the band gap for semiconductor nanoclusters occur.[1–4] The three-dimensional spatial confinement of the positron wave function in the nanoclusters is called *positron confinement*. Host-nanocluster systems that have been investigated very successfully are Li in MgO (Refs. 5 and 6) and Cu in Fe (Refs. 7 and 8). Here the Li and Cu nanoclusters adopt the unusual fcc Li and bcc Cu structures to be more coherent with the host matrix. The 2D-ACAR experiments in the works mentioned above provided a unique opportunity to investigate the Fermi surface of these unusual crystal structures. However, positron confinement only works when the positron affinity of the nanocluster is lower than the positron affinity of the host material and when the host-nanocluster interface is without defects so that the positron will not become trapped at the interface. Looking through the literature that has predicted positron affinity for almost all metals,[9] a number of semiconductors,[10] a few insulators,[5,11] and rare gases,[12] it is obvious that the solid noble gases have by far the lowest positron affinity of all elements (less than -10 eV), making them the most interesting candidates to further pursue and exploit the phenomenon of positron confinement. In this work, we have created solid Kr nanoclusters as observed by means of transmission electron microscopy (TEM) and investigated positron trapping in this host-nanocluster system. Solid Kr clusters created by means of ion implantation were already observed in the metals Ti, Ni, Cu, Mo, and Au,[13,14] in graphite and Grafoil,[15] and once in MgO.[16] Most of the work on solid Kr mentioned above concerns the analysis of diffraction patterns in TEM and x-ray absorption studies. We show solid Kr clusters in TEM in high-resolution mode, similar to the high-resolution work already performed on solid Xe clusters.[17]

II. EXPERIMENTS

Several epi-polished MgO(100) single crystals of size $10\times10\times1$ mm^3 were implanted at room temperature with 280 keV Kr ions to a dose of 3×10^{16} ions cm^{-2} and subsequently annealed in ambient air for periods of 30 min at temperatures of 900 K and 1100 K, respectively. After ion implantation and after each annealing step, the evolution of ion implantation defects was monitored with optical absorption spectroscopy and Doppler broadening positron beam analysis[18] (PBA) using a monoenergetic positron beam with a variable acceleration energy of 0–30 keV. Cross-sectional transmission electron microscopy (XTEM) was applied after the 1100 K annealing step. The TEM was performed using a JEOL 4000 EX/II microscope operating at 400 kV (point-to-point resolution 0.17 nm). The specimen preparation is dis-

TABLE I. Sample treatment and main experimental observations.

Sample treatment	
Ion implantation	3×10^{16} Kr ions cm^{-2} at an energy of 280 keV.
Thermal anneal	At 900 K and 1100 K for a period of 30 min.
Results	
Optical absorption	*F* and *V* centers present after implantation; dissociation after 900 K anneal.
XTEM	Cubical, solid Kr clusters at 70–130 nm depth, cluster size 2–4 nm. Cubical nanovoids at 15–30 nm depth, cluster size 2–5 nm.
PBA	Defect agglomeration during annealing. High *S* parameter in nanovoids layer; *S* parameter in Kr cluster layer higher than that of bulk MgO and lower than the *S* parameter of MgO with defects.

cussed elsewhere.[19] The sample treatment and main observations are listed in Table I.

III. RESULTS

First, the results of optical absorption spectroscopy will be presented. Next, the XTEM results will be shown, focusing both on the solid Kr nanoclusters and on the defects created in the MgO. Finally the result of positron beam analysis is shown as an additional method to obtain depth-resolved information on the defect evolution in the composite material during the sample treatment. Possible trapping in Kr nanoclusters is discussed in terms of the positron affinity.

A. Optical absorption spectroscopy

The results of the optical absorption spectroscopy are displayed in Fig. 1. After ion implantation, two types of defects can be distinguished. At a wavelength of 570 nm, there is an absorption peak that can be attributed to *V* centers (Mg vacancies) and at a wavelength of 250 nm, there is another absorption peak that can be attributed to *F* centers (O vacancies).[20] Both absorption peaks vanish after annealing at 900 K.

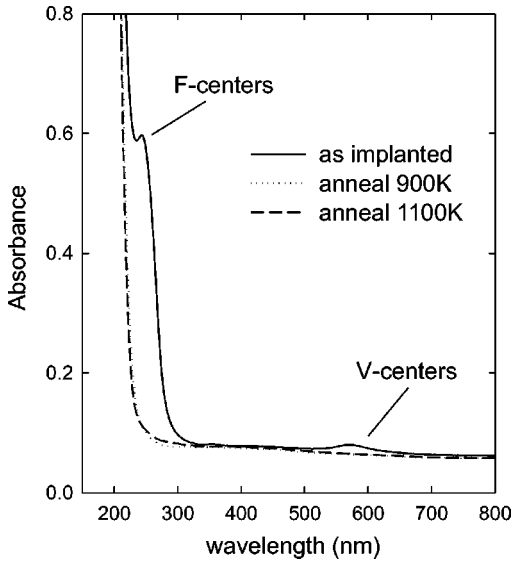

FIG. 1. Optical absorption spectra of a MgO(100) crystal implanted with 280 keV 3×10^{16} Kr ions cm^{-2}, as implanted and after annealing in air at various temperatures.

B. Cross-sectional TEM

XTEM was performed on a sample after the 1100 K anneal step. Figure 2 shows an overview image. The area between 70 and 130 nm depth is a subsurface layer that contains Kr nanoclusters. The rectangular area in Fig. 2 (marked with the white brackets) is enlarged in the high-resolution TEM image of Fig. 3. Here the Kr nanoclusters can be clearly observed. The clusters are rectangularly shaped and the sizes vary from 2 to 5 nm. Moiré fringes are present due to the lattice mismatch between solid Kr and MgO.

The morphology of the nanoclusters is determined by the interface energy corresponding to the various MgO‖Kr inter-

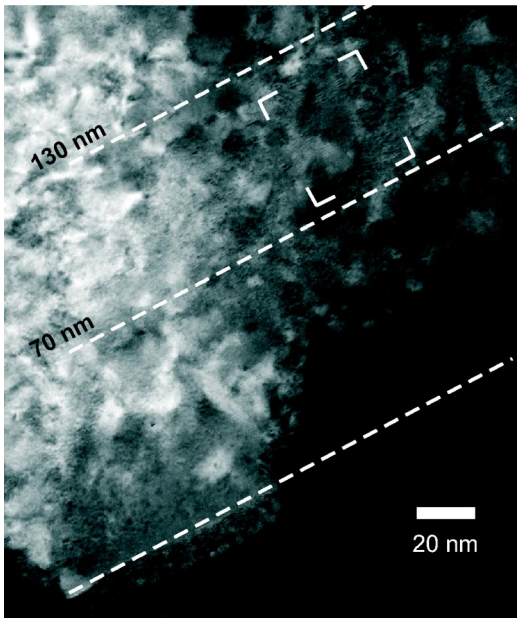

FIG. 2. TEM overview image of Kr-implanted MgO. Solid Kr nanoclusters are observed in a band at a depth of 70–130 nm. The white brackets indicate the area shown in Fig. 3.

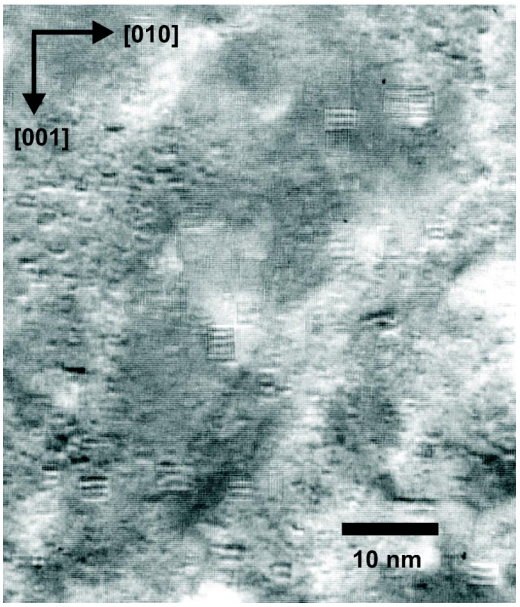

FIG. 3. Solid Kr nanoclusters at a depth of 75–120 nm with Moiré fringes caused by the lattice mismatch between solid Kr and MgO.

face facets; the shape of the cluster can be constructed using the Wulff diagram[21,22] if the interface energies are known. In this particular case, it is clear that the {100} interface is energetically more favorable than the {110} and {111} interfaces. The interface energy equals the sum of the surface energies of MgO and Kr minus the work of adhesion:

$$\gamma_{\mathrm{MgO}\|\mathrm{Kr}} = \gamma_{\mathrm{MgO}} + \gamma_{\mathrm{Kr}} - W_{\mathrm{ad}}. \tag{1}$$

Considering that the van der Waals bonding of the noble gas Kr atoms is very weak, the interface energy of Kr and the work of adhesion will be negligible with respect to the surface energy of MgO, i.e., by approximation the MgO‖Kr interface energy equals the MgO surface energy. Watson *et al.*[23] calculated surface energies of 1.25 $\mathrm{J\,m^{-2}}$ for MgO{100}, 1.87 $\mathrm{J\,m^{-2}}$ for MgO{110}, and 2.5 $\mathrm{J\,m^{-2}}$ for MgO{111}. The last two values are valid for microfaceted surfaces, but the surface energies for unfaceted {110} and {111} MgO surfaces are even higher.[23] Considering the Wulff diagram,[21,22] the absence of the {110} facets in the rectangular Kr nanoclusters means that the MgO{110} surface energy should be at least $\sqrt{2}$ times larger than the MgO{100} surface energy, which is in agreement with the theoretical values given above.

Figure 4 shows a magnification of the large cluster present in the center of Fig. 3. There are five Moiré fringes in 18 MgO lattice spacings. Since Kr is fcc in fcc host matrices[14] and the Kr clusters are in a cube-on-cube orientation relationship with the MgO, the following relationship can be used to calculate the lattice parameter of solid Kr, a_{Kr}:

$$\frac{1}{d_{\mathrm{fringes}}} = \left| \frac{1}{d_{\mathrm{MgO}}} - \frac{1}{d_{\mathrm{Kr}}} \right|. \tag{2}$$

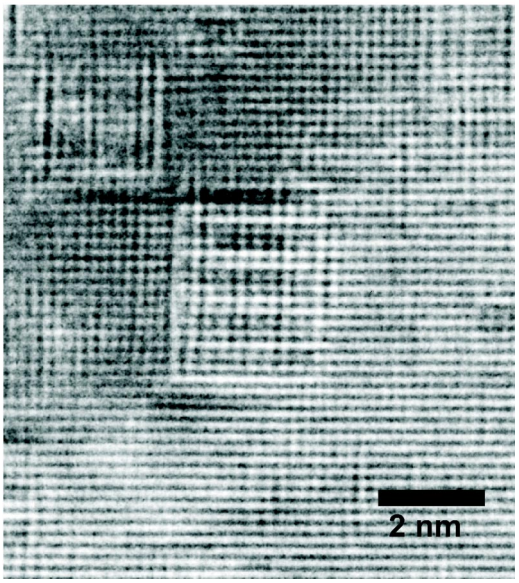

FIG. 4. High-resolution TEM image of a solid Kr nanocluster (also present in the center of Fig. 3). The lattice parameter of the solid Kr can be derived from the Moiré fringes (see text).

With a lattice parameter a_{MgO} of 4.212 Å ($d_{\mathrm{MgO,200}} = 2.106$ Å), this yields $d_{\mathrm{Kr,200}} = 18/(18-5)d_{\mathrm{MgO,200}} = 2.9$ Å and thus the lattice parameter for solid Kr, a_{Kr}, equals 5.8 Å. This corresponds to the lattice parameter of frozen Kr at a temperature of 110 K.[24] In a similar fashion, the Kr lattice parameters in the other clusters present in Fig. 3 can be analyzed and values of 5.3–5.8 Å are found. These values for a_{Kr} correspond reasonably well with values of 5.0–5.5 Å reported in the literature.[13,16] The important advantage of the use of Moiré fringes in comparison with the experimental methods mentioned in the Introduction is that the lattice parameter can be determined for every Kr cluster separately. In Fig. 5, the Kr lattice parameter is plotted as a function of the cluster size. It is clear that there is a positive correlation between a_{Kr} and the cluster size; the straight line plotted in

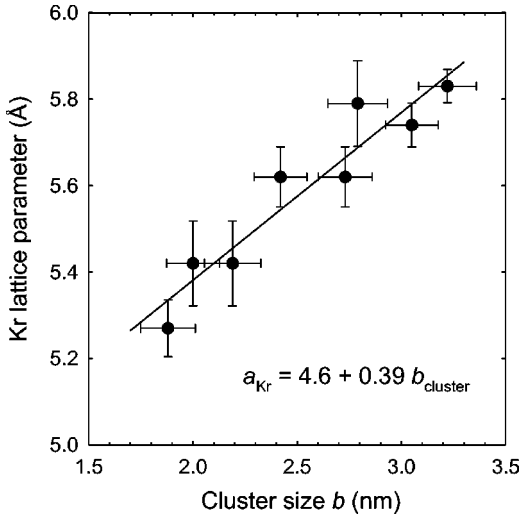

FIG. 5. Relationship between the Kr lattice parameter and the cluster size.

the figure is a linear least squares fit to the data. The cluster size (defined as the cube root of the nanocluster volume) cannot be determined accurately since the cluster dimension perpendicular to the plane in Fig. 3 or 4 cannot be determined. Therefore, the cluster size was estimated as the square root of the cluster area that is visible in the figures. The lattice parameter in small clusters is smaller due to the higher pressure in small clusters. The lattice parameter can be related to the pressure using the Ronchi equation of state (EOS). A lattice parameter of 5.3–5.8 Å for fcc Kr corresponds to a molar volume of 22–30 cm^3. Using the EOS for solid Kr at a temperature of 300 K,[25] the pressure in the largest cluster is 0.6 GPa and the pressure in the smallest cluster 2.5 GPa. These pressures are in reasonable agreement with the minimum pressure of 0.83 GPa that is necessary for the formation of solid Kr.[16] It is also in good agreement with the following equations, describing the relationship between pressure and interface energy. The energy of the cluster system is minimized when

$$dE = pdV - \gamma dS = 0 \Rightarrow \frac{dE}{da} = p\frac{dV}{da} - \gamma\frac{dS}{da} = 0. \qquad (3)$$

For the case of a cube with size b, volume $V=b^3$, and surface $S=6b^2$, it follows that

$$p = \frac{4\gamma}{b}. \qquad (4)$$

Since the interface energy is completely determined by the surface energy of MgO [see Eq. (1) and the discussion above], the pressure in the cluster can be calculated. It should be realized that Eqs. (3) and (4) are only valid when the material is in thermal equilibrium, i.e., at the temperature at which the clusters were formed. The pressure and surface energy mentioned in Eq. (4) should therefore be considered at 1100 K. The MgO{100} surface energy at 1100 K is 1.17 $J\,m^{-2}$ (Ref. 26). Using Eq. (4), a cluster size of 3 nm then yields a pressure of 1.7 GPa at 1100 K. How can this pressure be compared with the pressures of 0.6–2.5 GPa found in the electron microscope at 300 K? MgO is a rather incompressible material with a linear thermal expansion coefficient that varies with temperature. Over the temperature interval of 300–1100 K, the average linear thermal expansion coefficient a_{lin} is $12\times10^{-6}\ K^{-1}$ (Ref. 27). Since MgO is very incompressible compared to Kr, we assume that the shrinkage of the cluster is completely determined by MgO. With $a_{vol}=3a_{lin}$, the change in volume of the cluster is 2.9%. Therefore, the molar volumes of 22–30 cm^3 as found at room temperature correspond to molar volumes of 23–31 cm^3 at 1100 K. Using again the Ronchi equation of state,[25] but now for a temperature of 1100 K, we find pressures of 1.5–4.6 GPa. This is in good agreement with the pressure of 1.7 GPa that was found from Eq. (4).

Figure 6 shows an enlarged TEM image of the subsurface area down to a depth of 60 nm. It is clear that a band of rectangularly shaped nanovoids is present at a depth of 15–30 nm. These large vacancy clusters are 2–5 nm in size and are rectangularly shaped, similar to the nanovoids found previously in ion-implanted MgO.[28] The rectangular shape is again caused by the different surface energies of the various

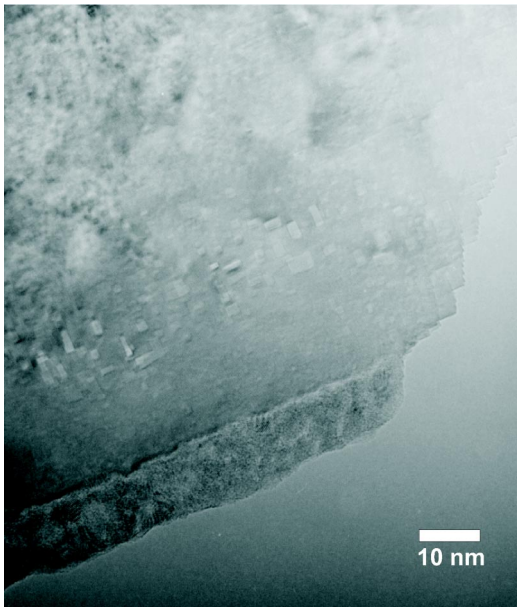

FIG. 6. TEM image showing the vacancy cluster band located at a depth of 15–30 nm.

MgO facets (see the discussion above on the rectangular shape of the Kr clusters). These voids are formed due to accumulation of vacancies created by the Kr implantation. It is, however, peculiar that this vacancy band is located so far away from the main Kr cluster band, since normally the damage depth distribution and the Kr depth distribution from the same implantation are overlapping to a large extent.

Figure 7 shows the Kr depth distribution and the damage created by ion implantation as simulated by means of the SRIM2000 code (Stopping and Range of Ions in Matter).[29] Here displacement energies of 55 eV were used for both Mg and O.[30] For the applied dose of 3×10^{16} ions cm^{-2}, the peak value of the Kr concentration is 4.1 at. % and the peak

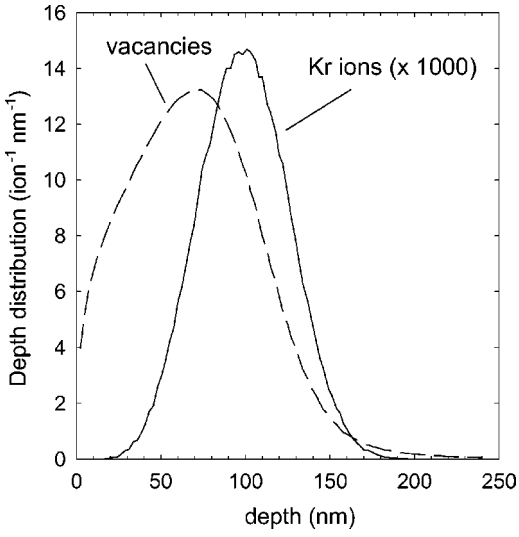

FIG. 7. Kr depth distribution (after implantation, prior to thermal anneal) and damage depth distribution as calculated using the SRIM2000 code (Ref. 29).

damage level is 37 dpa (displacements per target atom). First, it is clear that the predicted Kr depth distribution is in excellent agreement with the location of the Kr nanocluster layer at a depth of 70–130 nm as observed by TEM in Fig. 2. It is also clear that the predicted damage depth distribution is located shallower than the predicted Kr distribution. However, this does not explain the presence of a distinct vacancy cluster band at a depth of 15–30 nm as observed by TEM: in the SRIM simulation the vacancy and Kr distribution are not separated but overlap to a large extent. A possible explanation is that the vacancies and Kr atoms recombine at the intermediate depth range of 30–70 nm: the presence of Kr in the vacancy clusters slows down the mobility of Kr-filled vacancy clusters so that large vacancy clusters are not formed. At the same time, the concentration of Kr in this intermediate layer is not high enough to form solid Kr nanoclusters that are large enough to be observed by means of TEM.

C. Positron beam analysis

The defect evolution during the annealing procedure was monitored by Doppler broadening PBA.[18] Annihilation of positrons with electrons in solids yields information on the momentum distribution of these electrons. The electronic momentum distribution is reflected in the Doppler broadening of the 511 keV annihilation peak. Positron annihilation with low-momentum valence or conduction electrons results in a small Doppler shift, contributing to the center of the peak. Annihilation with high-momentum core electrons results in a large Doppler shift, contributing to the wings of the 511 keV annihilation peak. The shape of the 511 keV peak is characterized by the so-called *S* (shape) parameter, which gives the ratio of the number of counts in the center of the peak to the number of counts in the whole peak.[18,5] By using a monoenergetic positron beam with variable energy, the *S* parameter can be recorded as a function of depth. However, at larger depths the depth resolution decreases due to broadening of the implantation profile of the implanted positrons.

The *S* parameter is displayed in Fig. 8 as a function of positron implantation energy. The average positron implantation depth is indicated on top of the figure. The solid lines show the results of the VEPFIT simulation that will be discussed below. It is clear that after implantation, the *S* parameter increases with respect to reference MgO in the ion-implantation zone and it increases further after annealing at 900 K and 1100 K over a wide range. The *S* parameter in ion-implanted MgO always increases after ion implantation due to the efficient formation of vacancy-type defects in the Schottky material MgO.[28] It is observed that the *S* parameter increases after annealing at 900 K. Simultaneously, the optical *F* and *V* centers dissociate after annealing at this temperature as observed with optical absorption spectroscopy (see Fig. 1). This clearly indicates aggregation of vacancy-type defects (the larger the vacancy clusters, the larger the *S* parameter). The peak at 1.5 keV positron implantation energy in Fig. 8 can be attributed to the presence of the vacancy cluster band that was observed with TEM in Fig. 6. These voids are large enough to form positronium (Ps), a hydrogen-like bound state of a positron (e^+) and an electron (e^-). Positronium formation leads to a dramatic increase in the *S* parameter.[18] In order to analyze the PBA results in more detail, the VEPFIT code[31] was used to find the *S* parameter corresponding to every defect layer. The *S* parameter found at certain positron energy in Fig. 8 consists of contributions of various layers due to the broadness of the positron implantation profile (which is increasing with increasing positron energy) and due to positron diffusion processes. The VEPFIT code takes these effects into account and yields the depth-resolved *S* parameters for every defect layer. Based on the TEM observations, a six-layer model was used as defined in Table II. The chosen diffusion lengths are reasonable estimates. When considering the number of clusters in Figs. 3 and 6, it is clear that here the diffusion length will be 5 nm or less. The layers and the corresponding depths are indicated at the top of the graph in Fig. 8. Layer V with a depth of 130–300 nm is the so-called ion-implantation tail. Due to channeling effects, the implantation damage in MgO extends much further than the maximum range as predicted by SRIM (Fig. 7) as this code assumes the atoms in the target material to be randomly distributed. Only for the *S* parameter curve of reference (nonimplanted) MgO, a single-layer model was used with the *S* parameter value of bulk MgO, 0.475.

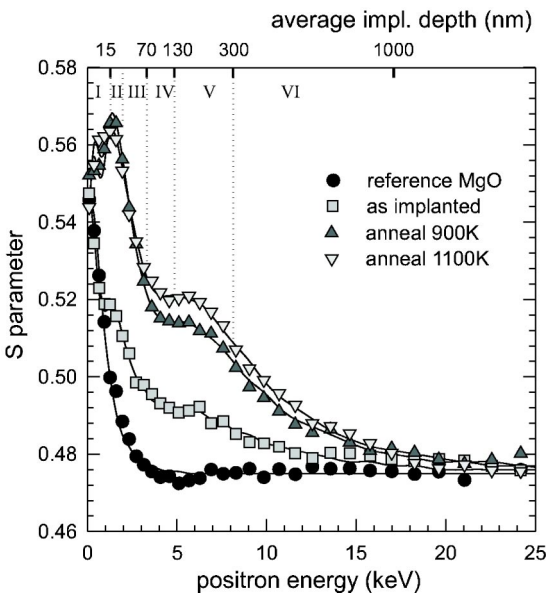

FIG. 8. *S* parameter vs positron energy measured for reference MgO and for MgO:Kr after implantation and after thermal annealings. The scale at the top of the graph indicates the average positron implantation depth. The Roman numerals are the layer numbers (see Table II) and the solid lines are the result of VEPFIT fitting (see text).

The solid lines in Fig. 8 are the result of VEPFIT fitting and it is clear that the model as discussed above is well able to fit the experimental *S* parameter curves. Figure 9 shows the depth-resolved *S* parameters found using VEPFIT for the sample after the 1100 K annealing step (where XTEM was also performed). As expected, the *S* parameter in the nanovoids layer (layer II) is rather high, 0.59. The *S* parameter in the layer with Kr nanoclusters (layer IV) is lower than that of

TABLE II. Model used for VEPFIT simulation. Note that the *S* parameters of layers I, III, and V are fitted with the same parameter.

Layer	Description	Depth (nm)	*S* par.	Diff. length (nm)
I	MgO with defects	0–15	S_{def} (fitted)	5
II	nanovoids	15–30	S_{voids} (fitted)	5
III	MgO with defects	30–70	S_{def} (fitted)	5
IV	Kr clusters	70–130	S_{Kr} (fitted)	5
V	MgO with defects	130–300	S_{def} (fitted)	20
VI	MgO bulk	>300	$S_{\mathrm{MgO}}=0.475$	100

the adjacent layers but higher than that of bulk MgO. This explains the ''dip'' in the *S* parameter curve in Fig. 8 at 4.5 keV positron implantation energy. The fact that the *S* parameter in the layer with Kr nanoclusters is not much different from adjacent layers points to the low interaction of positrons with Kr nanoclusters. The reason that the *S* parameter in the nanocluster layer is lower than in the adjacent layers (Figs. 8 and 9) is probably due to Kr filling of vacancy-type defects. Thus there are less open volume defects for the positrons to become trapped in and the value of the *S* parameter is closer to that of bulk MgO.

In order to investigate the behavior of positrons with respect to the nanoclusters in more detail, a 2D-ACAR experiment was carried out on the nanoclusters after the 1100 K annealing step. 2D-ACAR allows a detailed investigation of the electronic structure of a material.[32,8,6] Experimental details of the setup can be found in Refs. 5 and 6, where positron confinement in Li nanoclusters in MgO is investigated. The positrons were implanted at 4.5 keV energy, corresponding to implantation in the center of the Kr nanocluster layer. No anisotropic contribution other that that of MgO could be observed in the 2D-ACAR spectrum after accumulation of 7×10^6 2γ-coincidence events,[33] thus supporting the idea of negligible trapping in and interaction with Kr clusters. This is in contradiction with the expectation that positrons are very effectively trapped in Kr nanoclusters because of the very low positron affinity of solid Kr (Ref. 12) compared to that of MgO.[5] So why do the Doppler broadening and 2D-ACAR results not give evidence of positron trapping in the Kr nanoclusters?

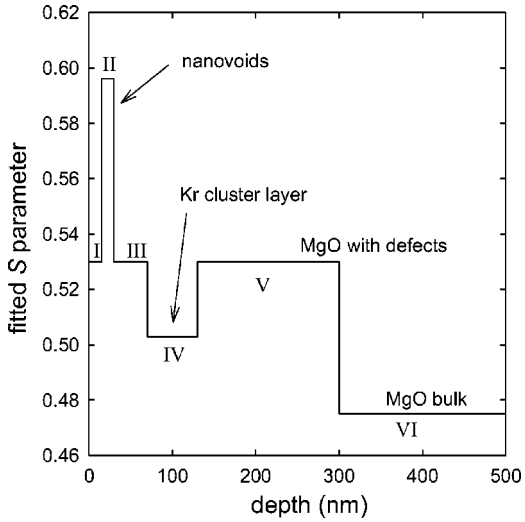

FIG. 9. Depth-resolved *S* parameter as a function of depth in the sample after the 1100 K annealing step, as found using the VEPFIT code. The applied six-layer model is given in Table II. The layers are indicated in Roman numerals.

D. Positron trapping and positron affinities

Whether positrons become trapped in nanoclusters is dependent on the positron affinity.[9,7,5] First we deduce the definition of positron affinity for metals, following the derivation by Puska and co-workers.[9,34] Let us first consider Fig. 10. Both the electronic energy levels and the positronic energy levels in the same material are defined with respect to the crystal zero (CZ). The crystal zero level is defined as the Coulomb potential far away from a single atomic sphere.[34] The electron chemical potential μ_- is defined as the energy difference between the top of the conduction band (coinciding with the Fermi level) and the crystal zero. The positron chemical potential μ_+ is defined as the energy difference between the bottom of the positron bands $E_{+,0}$ and the crystal zero. Both μ_- and μ_+ are usually negative. The electronic work function ϕ_- (positron work function ϕ_+) is the work to be done to bring an electron (positron) from the Fermi level (positron ground level) to vacuum. The surface dipole potential step Δ is the potential difference for electrons between the vacuum level and the crystal zero. Positrons experience the same potential step, but then with opposite sign: $-\Delta$. The following relationships hold:

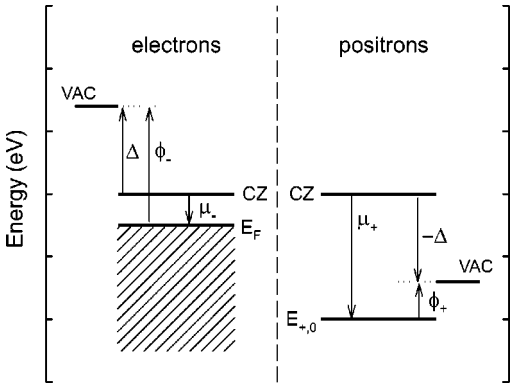

FIG. 10. Schematic diagram showing the relevant electronic and positronic energy levels with respect to the crystal zero (CZ) for the case of a metal.

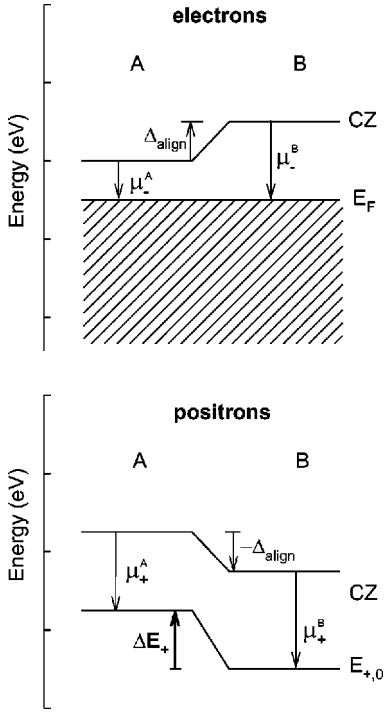

FIG. 11. Schematic diagram showing alignment of the Fermi levels for the case of two metals in contact. Note that the alignment shift of the crystal zeros is $\Delta=\mu_-^A-\mu_-^B$ for electrons and $-\Delta$ for positrons.

$$\phi_-=-\mu_-+\Delta, \tag{5a}$$

$$\phi_+=-\mu_+-\Delta. \tag{5b}$$

When two metals surfaces are in contact, electrons will flow from one material to the other until the Fermi levels are aligned, thereby establishing thermal equilibrium. This situation is shown in Fig. 11. The result is an interface dipole with potential difference $\Delta_{\text{align}}^{\text{METAL}}=\mu_-^A-\mu_-^B$. For positrons, this potential step is equal in magnitude but opposite in direction. The difference between the lowest positron energies of material A and B equals[9]

$$\Delta E_{AB,+}^{\text{METAL}}=E_{0,+}^A-E_{0,+}^B=\mu_+^A-\mu_+^B+\mu_-^A-\mu_-^B, \tag{6}$$

which is also clear from Fig. 11. When the positron affinity is defined as

$$A_+^{\text{METAL}}=\mu_++\mu_-=-(\phi_++\phi_-), \tag{7}$$

it follows from Eq. (6) that the difference in positron ground levels between the two metals is simply the difference between the positron affinities,

$$\Delta E_{AB,+}=A_+^A-A_+^B. \tag{8}$$

Values for the positron affinity are commonly expressed in eV and are negative for most materials. The positron affinity is an entity that is characteristic of a material and it has been calculated for almost all metals,[9] a number of semiconductors,[10] a few insulators,[5,11] and rare gases.[12] A necessary condition of the positron quantum confinement in a cluster (A) embedded in a host (B) is that $\Delta E_{AB,+}<0$. Then the cluster represents a three-dimensional potential well for positrons.[5] If $\Delta E_{AB,+}>0$, the cluster acts as a potential barrier. Finally, the possibility should be considered that positrons are trapped at the interface.

The question now arises whether the concept of positron affinity as defined in Eq. (7) can be applied to an insulator-insulator interface. The alignment of the Fermi levels is expressed in the term $\mu_-^A-\mu_-^B=\Delta_{\text{align}}^{\text{METAL}}$ on the right-hand side of Eq. (6). This is true for metals where the position of the electronic chemical potentials coincides with the position of the Fermi levels. This is not true, however, for insulators. In insulators the electronic chemical potential is defined as the distance between the top of the valence band and the crystal zero,[12] as depicted in Fig. 12. E_V is the top of the valence band, E_C is the bottom of the conduction band, and E_F is the Fermi level positioned in the middle of the band gap E_g. Figure 12 shows the electronic and positronic energy levels

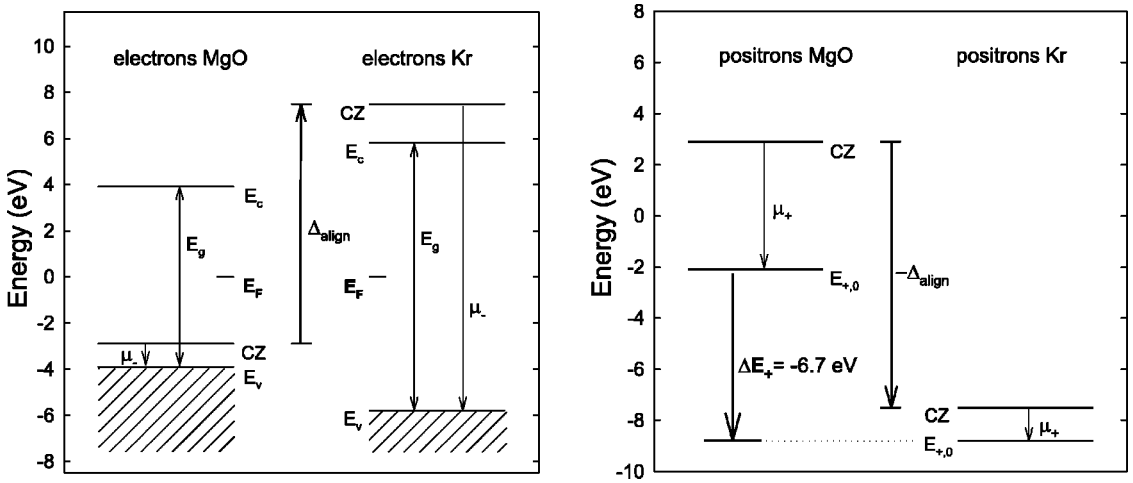

FIG. 12. Electronic and positronic energy levels for MgO in contact with solid Kr, based on the data listed in Table III. The alignment of the Fermi levels is achieved by an energy shift $\Delta_{\text{align}}^{\text{INS}}=\mu_-^A+\frac{1}{2}E_g^A-\mu_-^B-\frac{1}{2}E_g^B$ between the crystal zeros of the two materials.

TABLE III. Electronic and positronic data for MgO and Kr.

	MgO	Kr	Reference or equation
a_0 (Å)	4.212	5.72	Refs. 12, 41
μ_- (eV)	−1.0	−13.3	Refs. 12, 41
μ_+ (eV)	−5.0	−1.3	Refs. 12, 41
ϕ_- (eV)	3.8	11.9	Refs. 12, 39
ϕ_+ (eV)	2.2	2.7	Eq. (5b), Ref. 12
Δ (eV)	2.8	−1.4	Eq. (5a)
E_C (eV)	6.8	−1.7	Refs. 12, 41
E_g (eV)	7.8	11.6	Refs. 12, 41
E_F (eV) [a]	2.9	−7.5	$\mu_- + \frac{1}{2}E_g$
A_+^{METAL} (eV)	−6.0	−14.6	Eq. (7)
A_+^{INS} (eV)	−2.1	−8.8	Eq. (10)
$A_+^{\mathrm{VAC}} = -\phi_+$ (eV)	−2.2	−2.7	Eq. (11)

[a]Defined with respect to the crystal zero in Fig. 12.

for MgO and Kr in contact for the case that the Fermi levels are aligned. It follows from the figure that $\Delta_{\mathrm{align}}^{\mathrm{INS}} = \mu_-^A + \frac{1}{2}E_g^A - \mu_-^B - \frac{1}{2}E_g^B$. The energies and energy levels displayed in the figure are to scale. The numerical values of the electronic and positronic entities for MgO and Kr are listed in Table III and are mainly obtained from Refs. 5 and 12. Considering Fig. 12, it is clear that the difference between the positron ground potentials of the two materials is not described by Eq. (6), but by the following formula:

$$\Delta E_{AB,+}^{\mathrm{INS}} = E_+^A - E_+^B = \mu_+^A - \mu_+^B + \mu_-^A - \mu_-^B + \frac{1}{2}E_g^A - \frac{1}{2}E_g^B. \tag{9}$$

Therefore, the positron affinity for insulators can be defined alternatively as

$$A_+^{\mathrm{INS}} = \mu_+ + \mu_- + \frac{1}{2}E_g, \tag{10}$$

so that Eq. (8) is still valid. Using Eq. (9) and the values given in Table III, we find a difference in positron ground potentials $\Delta E_{AB,+}^{\mathrm{INS}}$ of −6.7 eV. So $\Delta E_{AB,+} < 0$ and the Kr nanoclusters should act as potential wells, in contradiction with our experimental observations that do not show evidence of positron trapping in Kr.

One possible explanation is that the Fermi levels are not equalized. MgO and Kr are both insulators with large band gaps of 7.8 and 12 eV,[12] respectively. When there are no electrons available to align the Fermi levels, thermal equilibrium cannot be established and the vacuum levels will be aligned instead.[35] In addition, it is well known that the energy levels of rare-gas solids physisorbed on various metal surfaces are aligned to the vacuum level.[36–38] Therefore, we have also considered alignment of the vacuum levels. This is achieved analogous to the alignment procedure shown in Fig. 12. The final result is that the difference between the positron ground states of the two materials is simply the difference between the positron work functions,

$$\Delta E_{AB,+}^{\mathrm{VAC}} = -(\phi_+^A - \phi_+^B), \tag{11}$$

so that $-\phi_+$ takes the role of the positron affinity when the vacuum levels are aligned [compare with Eq. (8)]. With the values given in Table III, this yields −0.5 eV for $\Delta E_{AB,+}^{\mathrm{VAC}}$, indicating that the nanocluster still acts as a (shallow) potential well. However, the differences in calculated energies between various theoretical models are approximately 1 eV.[12,5] Furthermore, we have combined experimental and theoretical results, and the electronic and positronic data for Kr given in Table III are only valid for a lattice parameter of 5.72 Å, while in reality there is a distribution. Therefore, we estimate the systematic error in $\Delta E_{AB,+}$ to be at least 1.5 eV, so that it is not clear whether positrons will trap in Kr nanoclusters when the vacuum levels are aligned. The various possibilities for alignment of the electronic energy levels and the corresponding differences in positronic ground potentials are summarized in Table IV.

One more aspect to be considered is that Kr is commonly used as a moderator because positrons thermalize ineffectively in solid rare gases.[40] This means that positrons hardly loose energy when moving in ''bulk'' solid Kr. So even if the Kr nanoclusters would act as a potential well, a positron entering a nanocluster might not loose enough energy to be thermalized and to remain trapped inside the cluster until annihilation. In the literature, trapping in spherical Kr bubbles in metal (Ni, Cu) is reported[42,43] and these authors conclude that the trapping occurs at the interface rather than in the nanocluster itself. We cannot fully exclude that positrons are also trapped at the MgO‖Kr interface, but it is not likely. First, the TEM results suggest that the cubically shaped Kr clusters fit very well in the MgO lattice, reducing the probability of interface defects that can act as trapping sites. Second, if the positrons would trap at the interface, one would still expect an anisotropic contribution from Kr to the 2D-ACAR spectrum due to overlap of the positron wave

TABLE IV. Positronic potential difference between the Kr cluster and MgO in contact assuming alignment of the Fermi levels in metals [Eq. (6)], in insulators [Eq. (9)], or assuming alignment of the vacuum levels [Eq. (11)]. The data of Table III have been used to calculate the numerical values.

Level alignment	$\Delta E = E_+^{\mathrm{Kr}} - E_+^{\mathrm{MgO}}$	Result (eV)
Fermi (metals)	$\Delta E_+^{\mathrm{METAL}} = (\mu_+^{\mathrm{Kr}} + \mu_-^{\mathrm{Kr}}) - (\mu_+^{\mathrm{MgO}} + \mu_-^{\mathrm{MgO}})$	NA [a]
Fermi (insulators)	$\Delta E_+^{\mathrm{INS}} = (\mu_+^{\mathrm{Kr}} + \mu_-^{\mathrm{Kr}} + \frac{1}{2}E_g^{\mathrm{Kr}}) - (\mu_+^{\mathrm{MgO}} + \mu_-^{\mathrm{MgO}} + \frac{1}{2}E_g^{\mathrm{MgO}})$	-6.7 ± 1.5
Vacuum	$\Delta E_+^{\mathrm{VAC}} = (-\phi_+^{\mathrm{Kr}}) - (-\phi_+^{\mathrm{MgO}})$	-0.5 ± 1.5

[a]Not applicable: Does not apply to the MgO‖Kr insulator-insulator interface.

functions with the solid Kr. Unfortunately, the anisotropy in the electronic/positronic structure for bulk Kr is not known theoretically nor experimentally, so that we cannot analyze our experimental results into more detail.

IV. CONCLUSIONS

Solid Kr nanoclusters were successfully created in MgO by means of 280 keV Kr ion implantation and subsequent thermal annealing at 1100 K. The nanoclusters were observed by cross-sectional transmission electron microscopy (XTEM) in high-resolution mode. The fcc Kr nanoclusters are rectangularly shaped with sizes of 2 to 4 nm. The lattice parameters of the solid Kr in the clusters varies from 5.3 Å for small clusters to 5.8 Å for large clusters, with the lattice parameter increasing with increasing nanocluster size. Using the Ronchi equation of state (EOS), this corresponds to local pressures of 0.6–2.5 GPa. Both optical absorption spectroscopy and Doppler broadening positron beam analysis show that small defects are present in the MgO after the ion implantation and that defect aggregation occurs during annealing. Experimentally, no evidence was found for positron confinement in Kr nanoclusters. The nonequalization of Fermi levels, the poor thermalization of positrons in solid Kr, and the absence of trapping sites at the Kr‖MgO interface might be the reason why positrons are not trapped in Kr clusters.

[1] W. P. Halperin, Rev. Mod. Phys. **58**, 533 (1986).

[2] *Metal Clusters*, edited by W. Ekardt (Wiley, New York, 1999).

[3] *Semiconductor Nanoclusters*, edited by P. V. Kamat and D. Meisel (Elsevier, New York, 1997).

[4] A. P. Alivisatos, Science (Washington, D.C., U.S.) **271**, 933 (1996).

[5] M. A. van Huis, A. van Veen, H. Schut, C. V. Falub, S. W. H. Eijt, P. E. Mijnarends, and J. Kuriplach, Phys. Rev. B **65**, 085416 (2002).

[6] C. V. Falub, P. E. Mijnarends, S. W. H. Eijt, M. A. van Huis, A. van Veen, and H. Schut, Phys. Rev. B **66**, 075426 (2002).

[7] Y. Nagai, M. Hasegawa, Z. Tang, A. Hempel, K. Yubuta, T. Shimamura, Y. Kawazoe, A. Kawai, and F. Kano, Phys. Rev. B **61**, 6574 (2000).

[8] Y. Nagai, T. Chiba, Z. Tang, T. Akahane, T. Kanai, M. Hasegawa, M. Takenaka, and E. Kuramoto, Phys. Rev. Lett. **87**, 176402 (2001).

[9] M. J. Puska, P. Lanki, and R. M. Nieminen, J. Phys.: Condens. Matter **1**, 6081 (1989).

[10] B. K. Panda, G. Brauer, W. Skorupa, and J. Kuriplach, Phys. Rev. B **61**, 15 848 (2000).

[11] J. Kuriplach, W. Anwand, G. Brauer, and W. Skorupa, Appl. Surf. Sci. **194**, 84 (2002).

[12] M. J. Puska and R. M. Nieminen, Phys. Rev. B **46**, 1278 (1992).

[13] J. H. Evans and D. J. Mazey, J. Phys. F: Met. Phys. **15**, L1 (1985); Scr. Metall. **19**, 621 (1985).

[14] J. H. Evans and D. J. Mazey, J. Nucl. Mater. **138**, 176 (1986).

[15] Z. Tan, J. I. Budnick, D. M. Pease, and F. Namavar, Phys. Rev. B **43**, 1987 (1991).

[16] M. G. Norton, C. B. Carter, E. L. Fleischer, and J. W. Mayer, J. Mater. Res. **7**, 3171 (1992).

[17] R. C. Birtcher, S. E. Donnelly, M. Song, K. Furuya, K. Mitsuishi, and C. W. Allen, Phys. Rev. Lett. **83**, 1617 (1999).

[18] A. van Veen, H. Schut, and P.E. Mijnarends, in *Positron Beams and their Applications*, edited by P. Coleman (World Scientific, Singapore, 2000), Chap. 6, p. 191.

[19] B. J. Kooi, A. van Veen, J. Th. M. de Hosson, H. Schut, A. V. Fedorov, and F. Labohm, Appl. Phys. Lett. **76**, 1110 (2000).

[20] Y. Qian, D. Ila, R. L. Zimmerman, D. B. Poker, L. A. Boatner, and D. K. Hensley, Nucl. Instrum. Methods Phys. Res. B **127/128**, 524 (1997).

[21] H. Lüth, *Surfaces and Interfaces of Solid Materials*, 3rd ed. (Springer, Berlin, 1995), Sec. 3.1, p. 81.

[22] M. Backhaus-Ricoult, Acta Mater. **49**, 1747 (2001).

[23] G. W. Watson, E. T. Kelsey, N. H. de Leeuw, D. J. Harris, and S. C. Parker, J. Chem. Soc., Faraday Trans. **92**, 433 (1996).

[24] A. T. Macrander, Phys. Rev. B **21**, 2549 (1980).

[25] C. Ronchi, J. Nucl. Mater. **96**, 314 (1981).

[26] M. B. Taylor, C. E. Sims, G. D. Barrera, N. L. Allan, and W. C. Mackrodt, Phys. Rev. B **59**, 6742 (1999).

[27] H. Wengeler and F. Freund, CFI, Ceram. Forum Int. **58**, 31 (1981).

[28] A. van Veen, M. A. van Huis, A. V. Fedorov, H. Schut, F. Labohm, B. J. Kooi, and J. Th. M. De Hosson, Nucl. Instrum. Methods Phys. Res. B **191**, 610 (2002).

[29] J. F. Ziegler, J. P. Biersack, and U. Littmark, *The Stopping and Range of Ions in Solids* (Pergamon, New York, 1985). See also www.srim.org for information on updated versions.

[30] S. J. Zinkle and C. Kinoshita, J. Nucl. Mater. **251**, 200 (1997).

[31] A. van Veen, H. Schut, J. de Vries, R. A. Hakvoort, and M. R. IJpma, in *Positron Beams for Solids and Surfaces*, AIP Conf. Proc. **218**, edited by P. J. Schultz, G. R. Massoumi, and P. J. Simpson (AIP, New York, 1990), p. 171.

[32] R. N. West, in *Positron Spectroscopy of Solids*, edited by A. Dupasquier and A. P. Mills, Jr. (IOS Press, Amsterdam, 1995), p. 75.

[33] S. W. H. Eijt and C. V. Falub (private communication).

[34] O. V. Boev, M. J. Puska, and R. M. Nieminen, Phys. Rev. B **36**, 7786 (1987).

[35] A. Nagashima, N. Tejima, Y. Gamou, T. Kawai, and C. Oshima, Surf. Sci. **357-358**, 307 (1996).

[36] N. D. Lang and A. R. Williams, Phys. Rev. B **25**, 2940 (1982).

[37] J. Hulse, J. Kuppers, K. Wandelt, and G. Ertl, Appl. Surf. Sci. **6**, 453 (1980).

[38] K. Jacobi, Surf. Sci. **192**, 449 (1987).

[39] H. Namba and Y. Murata, J. Phys. Soc. Jpn. **53**, 1888 (1984).

[40] A. P. Mills, Jr. and E. M. Gullikson, Appl. Phys. Lett. **49**, 1121 (1986).

[41] Values obtained with the MgO II, generalized gradient approximation (GGA) model in Ref. 5.

[42] K. O. Jensen, M. Eldrup, N. J. Pedersen, and J. H. Evans, J. Phys. F: Met. Phys. **18**, 1703 (1988); K. O. Jensen, M. Eldrup, S. Linderoth, and J. H. Evans, J. Phys.: Condens. Matter **2**, 2081 (1990).

[43] D. T. Britton, P. C. Rice-Evans, and J. H. Evans, Philos. Mag. A **55**, 347 (1987).